Res Chem Intermed (2017) 43:2865–2880
DOI 10.1007/s11164-016-2798-y

Surface oxygen dynamics and H_2 oxidation on cobalt spinel surface probed by $^{18}O/^{16}O$ isotopic exchange and accounted for by DFT molecular modeling: facile interfacial oxygen atoms flipping through transient peroxy intermediate

Filip Zasada[1] · Janusz Janas[1] · Witold Piskorz[1] · Zbigniew Sojka[1]

Received: 27 June 2016 / Accepted: 24 October 2016 / Published online: 31 October 2016

Abstract Surface dynamics of reactive oxygen species (ROS) and hydrogen oxidation on cobalt spinel nanocatalyst, faceted predominantly with (100), were investigated by means of pulsed $^{16}O_2/^{18}O_2$ isotopic exchange and thermoprogrammed surface reaction investigations, corroborated by periodic spin-unrestricted DFT-PW91+U modelling of the principal surface reaction molecular events. Three temperature windows [$T < 350$ °C (i), 350 °C $< T <$ 700 °C (ii), and $T > 700$ °C (iii)] where identified and associated with diatomic oxygen species of superoxo (Co^O–$(O_2)^-$–Co^O, peroxo (Co^T–$(O_2)^{2-}$–Co^O) (i), and monoatomic metaloxo (Co^T–O, Co^O–O) nature (ii), and with oxygen vacancies V_O (iii). A new oxygen isotopic exchange pathway was proposed that involves peroxy transient intermediates produced during ROS oxygen surface diffusion. Flipping of the supra- (RSO) and intrafacial (lattice) oxygen moieties within the $[^{18}O_{sup}$–$^{16}O_{int}]^{2-}$ peroxy unit requires 0.39 eV only, opening an easy pathway for rapid isotopic exchange without explicit formation of energetically more costly oxygen vacancies. The latter may occur effectively at $T > 700$ °C. The catalytic activity of ROS species was probed by H_2 oxidation reaction. The diatomic ROS reactivity (below 160 °C) is characterized by $E_a = 16$ kcal/mol, and for monoatomic species (between 160 °C and 300 °C) it falls to $E_a = 9.2$ kcal/mol. It was shown that suprafacial dehydroxylation of ROS generated water is energetically less costly ($E_a = 1.15$ eV) than intrafacial dehydroxylation ($E_a = 1.71$ eV) entailing removal of water associated with the lattice oxygen. Thus, the former may operate even at relatively low temperatures (below 300–350 °C). The appearance of significant amount of $H_2^{16}O$ in the reaction products is related to easy isotopic $^{18}O/^{16}O$ scrambling via transient peroxo intermediates, and is not diagnostic of direct involvement of the Mars van Krevelen mechanism.

✉ Filip Zasada
zasada@chemia.uj.edu.pl

[1] Faculty of Chemistry, Jagiellonian University, ul. Ingardena 3, 30-060 Kraków, Poland

Keywords Reactive oxygen species · Co_3O_4 · Nanocrystal · Isotopic studies · DFT calculations

Introduction

Well-defined structure, facile shape tailoring and tuning of its electronic properties by iso- and heterovalent doping, make cobalt spinel oxide a unique model catalytic material, receiving recently a great deal of theoretical and practical attention [1, 2]. Co_3O_4 exhibits high activity in oxidation of carbon oxide [3], ammonia [4], methane, and other hydrocarbons [5, 6]. It is also well known for its spectacular activity in oxygen reduction reaction (ORR) [7], or low temperature decomposition of N_2O [8, 9]. High catalytic performance of cobalt spinel can be attributed to presence of various surface reactive oxygen species (ROS) stabilized on its surface in mild conditions and to easy formation of oxygen vacancies [10, 11]. It has been shown that for catalytic processes such as CO oxidation or N_2O decomposition the suprafacial reactive oxygen intermediates play a key role in the catalytic activity [12, 13]. In turn, the oxygen vacancies generated during catalytic reactions [14] or produced spontaneously at elevated temperatures [15] are often involved in the Mars-van Krevelen redox processes over cobalt spinel, exemplified, e.g., by oxidation of methane [16].

To design a catalytic system dedicated for particular application a detailed molecular level understanding of the reaction mechanism is indispensable. One of the crucial functionalities of the catalyst in various oxidation reactions is activation of dioxygen, leading to production of surface reactive oxygen species, and the ability to facile formation of oxygen vacancies, providing a nucleophilic lattice oxygen available for various oxidation processes [17]. Although it is generally accepted that both lattice oxygen and ROS species may be involved in oxidation reactions, there is still a debate about the specific role they play therein. A common method for studying oxygen dynamics in an oxide catalyst is ^{18}O–^{16}O isotopic exchange with gas mass spectroscopic detection. In such experiments it is possible to differentiate between surface exchange, bulk diffusion, and fast diffusion along grain boundaries [18]. From the course of the oxygen exchange reaction, the way in which oxygen takes place in the catalytic processes may also be deduced [19]. Following pioneering work by Klier et al. [20], there are three conceivable parallel pathways for an oxygen molecule to exchange the atoms with the catalyst surface (i) exchange proceeds without direct involvement of lattice oxygen (R_0), (ii) only one of the atoms of a molecule is replaced (R_1), (iii) both atoms of a single dioxygen molecule are exchanged by lattice oxygens (R_2).

According to a generally adopted scheme [17, 21, 22], the interaction of the oxide catalyst with adsorbed oxygen involves electron transfer from the catalyst surface donor sites to the adoxygen, converting suprafacial $O_{2(ads)}$ into lattice O^{2-} anions via a sequence of the consecutive/parallel steps of oxygen reduction, diffusion, and dissociation until final incorporation into the oxide lattice:

$$O_{2(g)} \leftrightarrow O_{2(ads)} \leftrightarrow O^{-}_{2(ads)} \leftrightarrow O^{2-}_{2(ads)} \leftrightarrow 2O^{-}_{(ads)} \leftrightarrow 2O^{2-}_{(lattice)}$$

The distribution of isotopic exchange products among various oxygen species depends on the relative rates of the above mentioned events. Hence, a faster incorporation reaction and subsequent diffusion leads to $^{16}O_2$ as the dominant isotopomer. Faster dissociation of oxygen compared with oxygen incorporation results in cross-labelled $^{16}O^{18}O$.

In contrast to CO oxidation or N_2O decomposition over cobalt spinel that have recently been investigated quite extensively [13, 23–25], much less attention is paid to hydrogen oxidation. Taking into account that oxidative properties of Co_3O_4 are related to the presence of surface ROS species including surface oxygen vacancies, their elementary electroprotic reactivity can be probed in a neat way by model hydrogen oxidation reaction. In addition to the direct practical relevance of H_2 oxidation, it is of great importance to understand fully methane or volatile organic compounds (VOC) oxidation mechanism, where the redox and acid–base functionalities are coupled into electroprotic properties of the catalyst surface. In such reaction hydrogen acts as a source of electrons, accommodated on Co active sites, and protons adsorbed on Lewis base surface O^{2-} oxygen. Another virtue of hydrogen oxidation model studies is that they provide direct insight into surface dehydroxylation processes, which are ubiquitous step for closing catalytic cycles in oxidation of hydrocarbons. Furthermore, such investigations may also help in resolving mechanistic issues that are relevant for preferential oxidation of CO in excess H_2 (CO-PROX) [26].

Herein we address the problem of suprafacial/intrafacial dynamics and reactivity of surface oxygen species produced on model cobalt spinel catalysts by using pulse $^{16}O_2/^{18}O_2$ isotopic exchange and hydrogen oxidation as a suitable probes. Experimental studies were supported by spin resolved DFT+U modeling of the key molecular surface events on the most abundant (100) termination of cobalt spinel.

Experimental and computational details

Materials and characterization

Cobalt spinel samples were synthesized via pH-controlled precipitation method by addition of 1 M $(NH_4)_2CO_3$ to 1 M $Co(NO_3)_2$ solution in room temperature (to obtain pH = 9). The catalyst precursor was filtered, dried overnight (T = 100 °C), and calcined in air at 700 °C for 3 h to obtain a good crystalline spinel structure. Following our recent work, such treatment leads to formation of the stoichiometric spinel both in the bulk [27] and the surface regions [28]. Purity of cobalt spinel phase was confirmed by X-ray diffraction, using CuKα radiation by means of a Rigaku Miniflex X-ray diffractometer equipped with a DeTEX detector. Raman spectra were recorded with an inVia Renishaw spectrometer equipped with a Leica microscope and the 785 nm laser excitation.

Isotopic exchange and catalytic studies

The temperature programmed surface reactions (TPSR) were performed in the range of 25–500 °C, using a quartz flow reactor in a fully automated catalytic setup, operating under LabView environment, equipped with a QMS detector (Hiden Analytical HPR20). The experiments were carried out with 100 mg of the catalyst (sieve fraction of 0.2–0.3 mm) with the feed flow rate of 50 mL min^{-1} (25 mL min^{-1} of 5% $^{18}O_2$ in Ar, and 25 mL min^{-1} 5% H_2 in He), and the heating rate of 10 °C min^{-1}. The molar flow rates of reactants and products (μmol min^{-1}) were calculated on the basis of the QMS signals calibrated against the post-reactor argon trace of controlled flow. For isothermal $^{18}O_2$ pulse experiments an automatic Valco sampling valve with a 2.5 cm^3 loop was used for injections.

Molecular modeling

DFT+U calculations were performed using the VASP code with the Hubbard parameter $U = 3.5$ eV, following the literature [29]. The projector augmented plane wave method (PAW) together with the generalized gradient PW91 exchange-functional were employed. We used standard Monkhorst–Pack grid with $5 \times 5 \times 5$ sampling mesh for bulk calculations and $5 \times 5 \times 1$ for slab calculations. The cutoff energy was set to 500 eV, and the SCF convergence criterion to 10^{-5} eV. A systematic validation of the applied calculation scheme against the experimental data can be found in our previous paper [30]. Bulk cobalt spinel unit cell was obtained by optimization of the experimental cubic ($1 \times 1 \times 1$) unit cell ($a_{exp.} = 8.08$ Å) containing 56 ions ($Co_{24}O_{32}$) with full optimization of all internal degrees of freedom within the error of 10^{-4} eV. The optimal cell lattice constant was calculated via the Birch-Murnaghan equation of state as $a_{DFT} = 8.14$ Å. Following our recent work [28] for modeling of spinel activity we used a dominant stoichiometric (100) surface. We applied a (1×1) slab of 17 atomic layers (~ 17 Å of thickness) with a supercell composition $Co_{48}O_{64}$, and a vacuum separation of 20 Å. The atomic positions in the four top and four bottom layers were relaxed with criterion of 10^{-3} eV $Å^{-1}$. The nudged elastic band method (NEB) [31, 32] was used to locate transition states (TS) of the investigated surface molecular events. In all calculations, for each identified transition state five to nine NEB images (including the initial and final ones) were used.

Results

Catalyst characterization

The single phase composition and crystallinity of the cobalt spinel catalyst were confirmed by X-ray diffraction, using CuKα radiation and the results (Fig. 1a) are characteristic for the cobalt spinel structure analyzed within the cubic *Fd*-3*m* space group (24210-ICSD), revealing that no major structural differences induced by different temperature of calcination are present. The quality of the sample was

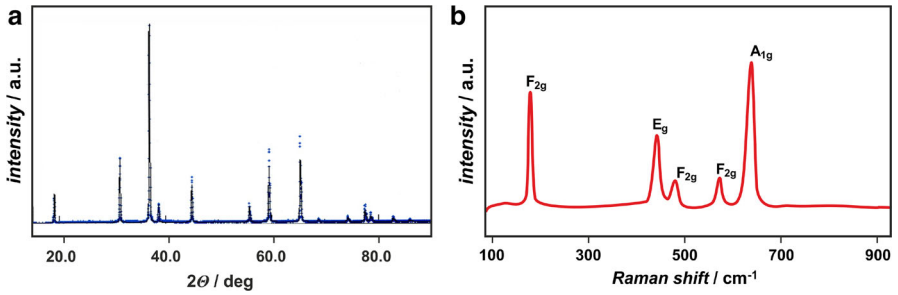

Fig. 1 XRD diffractogram (**a**) and Raman spectra (**b**) of the cobalt spinel sample

additionally verified by the micro-Raman techniques (Fig. 1b). The Raman spectra of cobalt spinel sample is characterized by five resolved Raman bands at about 194 (F_{2g}), 480 (E_g), 520 (F_{2g}), 620 (F_{2g}), and 690 (A_{1g}) cm^{-1}, predicted by the factor analysis [33], which also confirms absence of any minor spurious phases.

Further characterization details have been described in our recent papers [28, 30], where the HAADF-STEM pictures show that the Co_3O_4 nanocrystals expose predominantly the (100) facets. These results were used to develop a computational model, based on the most abundant (100) termination.

Pulse isotopic $^{18}O_2/^{16}O_2$ exchange and H_2 oxidation studies

The isotopic $^{18}O/^{16}O$ oxygen exchange pulse experiments performed at various temperatures are presented in Fig. 2. Below 300 °C upon $^{18}O_2$ pulses only small, practically constant, amounts of $^{18}O^{16}O$ were released. Formation $^{16}O^{16}O$ species was barely visible, indicating that surface oxygen dynamics is governed mainly by suprafacial processes. In such conditions dioxygen is present in a dinuclear forms stabilized on two vicinal octahedral Co ions (superoxo Co^O–($^{18}O^{18}O$)$^-$–Co^O) or on adjacent tetrahedral and octahedral Co (peroxo Co^T–($^{18}O^{18}O$)$^{2-}$–Co^O) centers, as described in detail in our previous paper [28]. For the sake of clarity in this notation only oxygen charge is given explicitly. The corresponding changes in the cobalt oxidation states are more involved as discussed elsewhere [28]. Whereas the Co^O–($^{18}O^{18}O$)$^-$–Co^O) species are stable at ambient temperatures only, the stability of the Co^T–($^{18}O^{18}O$)$^{2-}$–Co^O species extends over 200 °C. The diatomic species apparently are reluctant to isotopic exchange with the spinel surface, and only small amounts of the cross-labeled $^{16}O^{18}O$ species were observed in the temperature window of their stability. However, upon increasing of the reaction temperature above 300 °C the contribution of the $^{18}O^{16}O$ isotopomer gradually increases, reaching 50% of the original pulse intensity (Fig. 2). This effect is also reflected in pronounced enhancement of the $^{16}O^{16}O$ signal. Such behavior can be interpreted in terms of dissociation of the Co^T–($^{18}O^{18}O$)$^{2-}$–Co^O species into Co^T–$^{18}O^-$ and Co^O–$^{18}O^-$ mono-oxo entities:

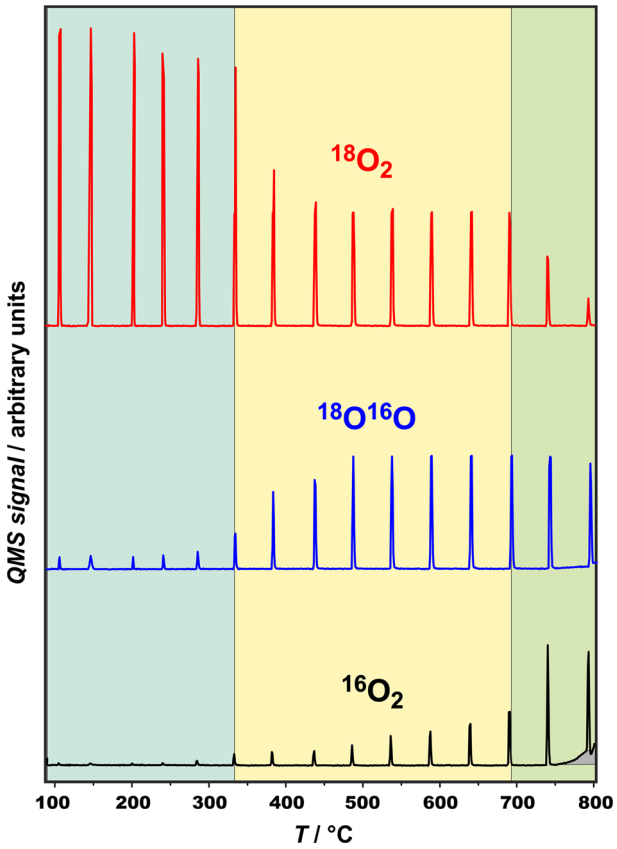

Fig. 2 Isotopic $^{18}O_2$ pulse experiments over Co_3O_4 catalyst performed at various temperatures showing formation of different dioxygen isotopomers ($^{16}O_2$, $^{18}O^{16}O$ and $^{18}O_2$)

$$Co^{T}-\left(^{18}O^{18}O\right)^{2-}-Co^{O} \rightarrow Co^{T}-{}^{18}O^{-}+Co^{O}-{}^{18}O^{-}$$

In the Co^{T}–$^{18}O^{-}$ adducts the oxygen adatom is rather strongly covalently bound, and is expected to be reluctant to isotopic exchange. The Co^{O}–$^{18}O^{-}$ species, however, are labile and the monoatomic oxygen can easily diffuse on the surface via transient peroxy $(^{16}O^{18}_{lattice}O)^{2-}$ species, as already observed and on alkaline earth oxides [34, 35]:

$$Co^{O}-{}^{18}O^{-}+{}^{16}O^{2-}_{lattice} \rightarrow Co^{O}+\left(^{16}O_{lattice}-{}^{18}O\right)^{2-}$$

Flipping of the both oxygen moieties in such species results in facile isotopic exchange:

$$\left(^{16}O_{lattice}-{}^{18}O\right)^{2-} \rightarrow \left(^{18}O_{lattice}-{}^{16}O\right)^{2-}$$

A more detailed molecular account of this process is discussed below. The surface peroxy can undergo recombination with adjacent oxygen adatoms (both peroxy and metaloxo species), leading in both cases to formation of gas phase $^{16}O^{18}O$.

$$\left(^{16}O_{lattice}-{}^{18}O\right)^{2-}+\left(^{18}O_{lattice}-{}^{16}O\right)^{2-}\rightarrow{}^{16}O^{2-}_{lattice}+{}^{18}O^{2-}_{lattice}+{}^{18}O^{16}O$$
$$\left(^{18}O_{lattice}-{}^{16}O\right)^{2-}+\ Co^{O}-{}^{18}O^{-}\rightarrow{}^{18}O^{2-}_{lattice}+\ Co^{O}+{}^{18}O^{16}O$$

Since the $^{16}O^{18}O$ response is well synchronized with the $^{18}O_2$ pulses, surface diffusion and the oxygen flipping within the peroxy transient intermediate must be fast within the experiment time scale. Above 700 °C the intensity of singly exchanged $^{16}O^{18}O$ (R_1) and doubly exchanged $^{16}O^{16}O$ species (R_2) dominate the intensity of the parent $^{18}O^{18}O$ pulse, which shows that at these conditions extensive interfacial isotopic R_1 and R_2 exchange between ROS and the surface O^{2-}_{surf} species takes place. This process should be, however, distinguished form gradual $^{16}O_2$ release due to oxygen vacancy formation (gray shaded area above 750 °C), which obviously is not paced by the $^{18}O_2$ pulses ($O^{\times}_{O} \rightarrow V_O + ½\ O_2$), in contrast to distinct response peaks of the $^{16}O^{16}O$ clearly induced by the $^{18}O^{18}O$ pulses only. Such behavior indicates that the $^{16}O^{18}O$ and the $^{16}O^{16}O$ response peaks are associated with rapid interfacial oxygen exchange involving peroxy intermediates, but not necessarily with explicit vacancy formation, usually implied in such conditions [36, 37]. Fast flipping of both the ^{18}O and ^{16}O moieties in the surface O_2^{2-} leads to efficient isotopic scrambling. Recombination of the atomic surface oxygen into dioxygen may then entail both ^{18}O and ^{16}O moieties leading to $^{16}O^{18}O$ formation.

The region below 350 °C, where the isotopic exchange of dioxygen in pulse experiment is small, was additionally probed by hydrogen oxidation reaction. The TPSR profiles of H_2 oxidation by $^{18}O_2$ (expressed as F/μmol min^{-1}) are presented in Fig. 3a, where three different stages of the reaction progress may by distinguished. At temperatures below 160 °C, the hydrogen conversion was low (<10%), and the reaction products were dominated by the $H_2^{18}O$ isotopomer. At ca. 160 °C the hydrogen decay profile falls down noticeably, which was accompanied by the concomitant enhanced production of both $H_2^{18}O$ and $H_2^{16}O$. Above 300 °C as the reaction approaches nearly 100% conversion the reaction progress due to lean conditions is determined by the reactants transport processes. These three stages of the hydrogen oxidation reaction were well reflected in the apparent activation energies, calculated from the associated Arrhenius plot (Fig. 3b**).** In the first region, the activation energy of hydrogen oxidation was equal to $E_a = 16$ kcal/mol, and it drops down to 9.2 kcal/mol in the second region, whereas above 300 °C the small value of $E_a = 2$ kcal/mol is characteristic of transport controlled process.

The observed regions can be accounted for by dynamic change in the nature of the reactive oxygen species on passing to higher temperatures, and by various extent of the water retention on the spinel surface as well. As discussed above, in the low temperature region, oxygen is adsorbed in the diatomic form that is resistant to isotopic exchange. Such species exhibit also rather low reactivity toward hydrogen, as implied by the relatively high activation energy of 16 kcal/mol. Upon moving to

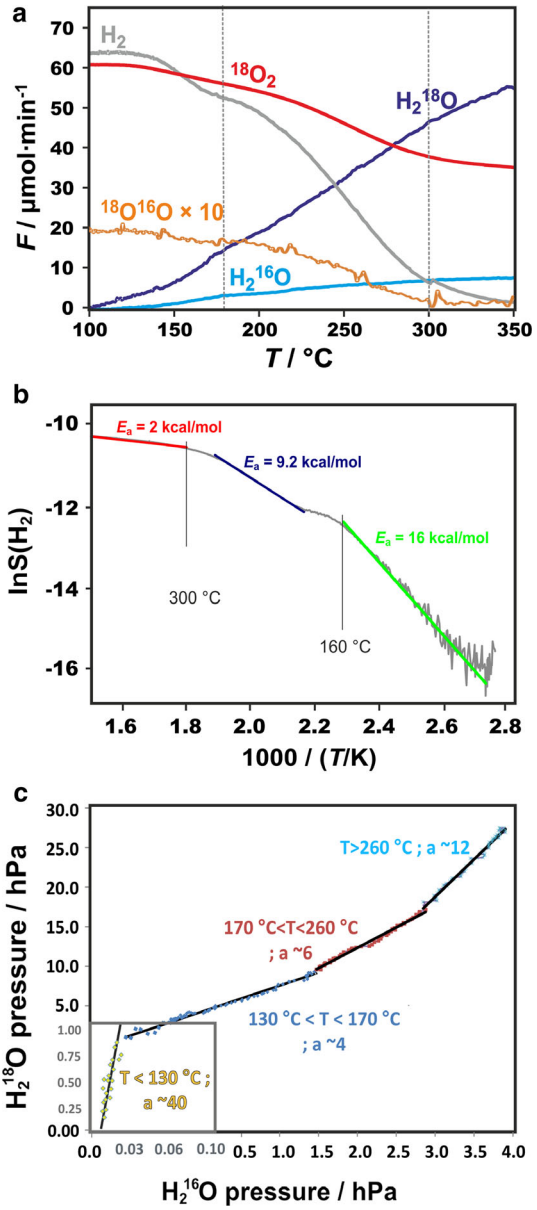

Fig. 3 The TPRS profile of hydrogen oxidation by isotopically labeled oxygen ($^{18}O_2$) showing the evolution of $H_2{}^{16}O$, $H_2{}^{18}O$, $^{18/18}O_2$, and H_2 reagents with temperature (**a**). Arrhenius-type plot of H_2 oxidation (**b**), and parity plot of water-16 versus water-18 partial pressures (**c**)

higher temperatures the dominant surface ROS are monoatomic oxygen entities. They are responsible for enhanced water production activating hydrogen more easily with E_a of 9 kcal/mol only. Since the oxygen monoatomic species are stable until 400 °C[28] they are responsible for hydrogen oxidation until full conversion is achieved (at 350 °C). In the whole investigated temperature range of hydrogen oxidation, formation of the $^{16}O^{18}O$ species was one order of magnitude

lower than that of $H_2^{16}O$. Moreover, whereas the $^{16}O^{18}O$ profile decreased the $H_2^{16}O$ one increased with the temperature. This indicates that the monoatomic ROS species produced on the spinel surface upon oxygen activation are overwhelmingly scavenged by the hydrogen.

The reaction progress was also influenced by retention of water molecules produced upon the hydrogen oxidation, as already mentioned. Following our previous investigations [38] adsorbed water is thermodynamically stable on the cobalt spinel surface at $p_{H2O} \sim 0.005$ atm. until $T \sim 150$ °C, thus part of the produced H_2O molecules may be retained in dissociative and associative forms. Dissociative forms of water exhibit ΔE_{ads} ranging from 1.18 eV to 0.89 eV, whereas adsorption energies of associatively attached H_2O are equal to 0.7 eV. From the thermodynamic diagram published previously [38] it may be thus expected that below 150 °C the most stable water forms are retained on the surface during catalytic reaction, leading to partial self-poisoning of the spinel surface by blocking the octahedral cobalt active sites. This gives rise to temporal stagnation of the catalytic activity around 180–200 °C, clearly seen in Fig. 3, as a deflection in the H_2 conversion profile. Above this temperature threshold, water leaves the surface, as manifested by a broad "desorption" peak on the both H_2O profiles, and the reaction rate is accelerated by the increasing temperature until 350 °C, where full hydrogen conversion was achieved.

The more detailed insight into water formation mechanism was provided by the $p_{H2(16)O}$ versus $p_{H2(18)O}$ parity plot presented in Fig. 3c. The detailed analysis shows that in the initial stage of the TPSR experiment ($T < 140$ °C) the $H_2^{18}O/H_2^{16}O$ ratio was equal to $f_{18/16}^{H2O} = 40$ and this value may be explained by suprafacial oxidation of hydrogen by diatomic oxygen species that are immobile; therefore, their enrichment in ^{16}O via oxygen flip within the peroxy intermediate is virtually impossible. Above 140 °C, once monoatomic oxygen species become dominant, the oxygen isotopic exchange through peroxy flipping mechanism becomes feasible, which is reflected in dramatic decrease in the $H_2^{18}O/H_2^{16}O$ ratio to $f_{18/16}^{H2O} = 4$.

From the catalyst mass and its BET surface we calculated the number of oxygen ions in first layer of Co_3O_4 (100) termination as 8.3×10^{18}. From the flow rates of ^{16}O containing products and the time of experiment we estimated the number of exchanged ^{16}O as 3.2×10^{20} in single TPSR run (50–350 °C). This results show that in given conditions, as the reaction proceeds the spinel surface may be gradually enriched in ^{18}O isotope to full coverage, making the interfacial oxygen-18 exchange into oxygen-16 less effective. This is reflected in the gradual increase of $f_{18/16}^{H2O}$ value with the progress of the reaction (increasing temperature).

Molecular modeling

The isotopic results of facile $^{18}O_2/^{16}O_2$ exchange and H_2 oxidation were accounted for by corroborative DFT modeling. Following our recent paper [30], we selected the most abundant stoichiometric (100) termination as a playground for the investigated molecular events.

Thermodynamic considerations reveals that in oxygen rich conditions, this surface may be covered by reactive oxygen species of different nature [28], and

among monoatomic species the metal-oxo form stabilized on the tetrahedral cobalt ion are the most stable (adsorption energy calculated versus O_2 molecule equals, $E_{ads} = -0.72$ eV). In the case of diatomic forms the peroxy nature Co^{T}–OO–Co^{O} configuration is the most stable ($E_{ads} = -1.22$ eV). In typical conditions of catalytic experiments ($p_{O2} = 0.01 \div 1$ atm) the former species is thermodynamically stable below 200 °C, whereas the latter from 200 °C to 400 °C. Above 400 °C the bare (100) surface of cobalt spinel is thermodynamically preferred. Since the monoatomic reactive oxygen species are essential in the investigated reactions (see below), we modeled the processes of dioxygen adsorption and subsequent activation leading to such adoxygen forms. The energetic profile and detailed molecular level description of dioxygen activation mechanism is presented in Fig. 4, where the initial configuration of the topmost layer (1×1) surface element of Co_3O_4 and gas phase O_2 is shown panel **a**. The surface cationic composition includes the octahedral pentacoordinated Co^{O}_{5c} ions (coded blue), topmost dicoordinated tetrahedral Co^{T}_{2c} (violet) and two concealed tetrahedral cobalt ions of full coordination (Co^{T}_{4c}, green), which are located in the first sublayer. The surface anionic composition (oxygen ions are marked in red) contains four truncated 3-fold coordinated oxygen ions (denoted as $O_{2O,1T}$) that are linked to two Co^{O} and to one Co^{T} cations, two 3-fold coordinated anions (O_{3O}) that are linked to the Co^{O} ions exclusively and two fully coordinated (fourfold) $O_{3O,1T}$ species. In transition state geometry (Fig. 4a$^{\#}$) the Co^{T}–O bond is nearly formed ($d_{Co-O} = 1.83$ Å), whereas the second bond (Co^{O}–O) is far from its optimal length ($d_{Co-O} = 2.51$ Å) and oxygen molecule is stretched

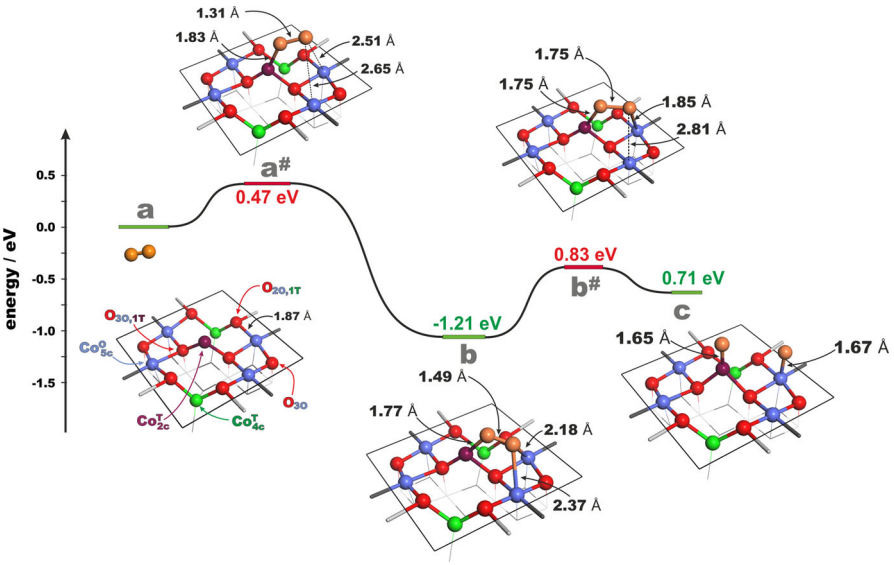

Fig. 4 The energetic profile of the adsorption and activation of dioxygen on the (100) plane. Each individual step is characterized by energy barrier (marked in *red*) and reaction energy (*green*), stable structures are labeled with *letters*, and the corresponding TS with additional # sign. The *color coding* is as follows: spinel oxygen: *red*, oxygen adatom: *orange*; exposed tetrahedral cobalt: *violet*, tetrahedral cobalt in first subsurface: *green*, octahedral cobalt: *blue*. (Color figure online)

from optimal 1.25–1.29 Å. Such geometrical strain is responsible for energy barrier for this step calculated as 0.47 eV. The resulting bidentate Co^T–OO–Co^O conformation (Fig. 4c), with the Co–O bonds of 1.77 Å and and O–O bond of 1.49 Å, is more stable than initial gas phase molecule by 1.22 eV. From this stable configuration, a step of the O–O bond breaking is required to produce monatomic oxygen species, and the transition state for this mechanism is presented in Fig. 4b$^{\#}$, where significant elongation of O–O bond (from to 1.49 to 1.75 Å) is visible. After the complete O–O bond breaking, the system optimize the geometry (Fig. 4e) and the resulting Co–O bond lengths of 1.65 Å (Co^T–O) and 1.67 Å (Co^O–O), indicates metal-oxo character of both species. The resulting monoatomic species are less stable than Co^O–OO–Co^O by 0.71 eV, but in the temperatures of the oxygen exchange and H_2 oxidation reaction they can easily diffuse on the surface, with formation of transient peroxy gropus. Such peroxy species constituting one reactive (top) and one lattice (bottom) oxygen are the most probable forms for straightforward isotopic exchange. Indeed, the ^{18}O–$^{16}O_{2O,1T}$ peroxy groups, which appear as transient intermediates during oxygen adatom diffusion along the Co^O and $O^{2-}_{2O,1T}$ sites:

$$\begin{aligned} {}^{18}O{-}Co^O{-}{}^{16}O^{2-}_{2O,1T}{-}Co^O &\rightarrow Co^O{-}\left({}^{18}O{}^{16}O_{2O,1T}\right)^{2-}{-}Co^O \\ &\rightarrow Co^O{-}O^{2-}_{2O,1T}{-}Co^O{-}{}^{18}O \end{aligned}$$

may constitute suitable platform for rapid oxygen isotopic exchange.

Indeed, once the $(^{18}O$–$^{16}O_{2O,1T})^{2-}$ peroxy entities are formed during the surface diffusion process, the top and down oxygen moieties can undergo easy flipping, exchanging the mutual positions of the suprafacial (top) and intrafacial (bottom) oxygen atoms (^{18}O–$^{16}O^{2-}_{2O,1T} \rightarrow {}^{16}O$–$^{18}O^{2-}_{2O,1T}$). The energetic profile of this process on the (100) surface is presented in Fig. 5. For each individual step taken into account the energy barrier (marked in red) and the reaction energy (green) were calculated. The consecutive stable structures appearing along the diffusion pathway are labeled with **a**, **b**, **c**, and **d** letters, and the corresponding transition states (TS) with an additional **#** sign. The starting structure (**a**) shows oxygen adatom (coded yellow) stabilized on the octahedral cobalt sites as metaloxo Co^O–$^{18}O^-$ entity with the bond length of 1.66 Å, which has been described previously [28, 39].

The oxygen adatom can be relocated to nearest $O_{2O,1T}$ anionic site through transition state (**a**$^{\#}$), (energy barrier of 0.72 eV), which can be described by slight elongation of the Co^O_{5c}–O bond ($\Delta d_{Co\text{-}O} = 0.1$ Å) and shortening of the O–$O_{2O,1T}$ distance (from $d_{O\text{-}O} = 2.71$ Å to 1.52 Å). Further evolution of the adoxygen leads to the formation of stable peroxy $(O$–$O_{2O,1T})^{2-}$ anion (**b**)**,** characterized by the O–O bond length of 1.41 Å. In this species one of the oxygen atoms is exposed above the surface plane (suprafacial oxygen), whereas the second O atom is located at the surface (intrafacial oxygen). The formed peroxy intermediate being less stable than the parent metal-oxo adduct by 0.41 eV may return to Co^O_{5c} (with E_a of 0.31 eV), restoring the starting configuration (**a**). It can also undergo a flip shown in the **b** → **b**$^{\#}$ → **c** sequence with quite small energy barrier of 0.39 eV. The latter scenario, resulting mainly from rearrangement of the cobalt–oxygen and the peroxy O–$O_{2O,1T}$ bonds by 0.2 and 0.1 Å, respectively, exchange the positions of the top

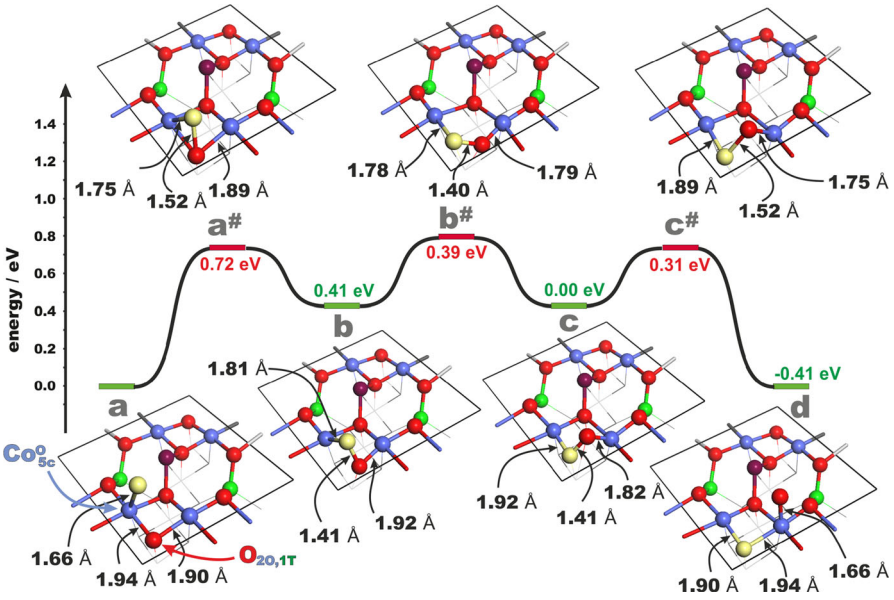

Fig. 5 The energetic profile of the diffusion mechanism of reactive oxygen species on the (100) plane between two adjacent octahedral cobalt sites. Each individual step is characterized by energy barrier (marked in *red*) and reaction energy (*green*), stable structures are labeled with letters, and the corresponding TS with additional # sign. The *color coding* is as follows: spinel oxygen: *red*, oxygen adatom: *yellow*; exposed tetrahedral cobalt: *violet*, tetrahedral cobalt in first subsurface: *green*, octahedral cobalt: *blue*. (Color figure online)

and the surface oxygen atoms, and is responsible for the facile suprafacial(^{18}O)/intrafacial(^{16}O) isotopic oxygen exchange. The isotopically scrambled peroxy anion can next be transformed into Co^{O}–$^{18}O^{-}$ metal-oxo adduct along the **c** → **c**$^{\#}$ → **d** sequence with activation energy of 0.31 eV, which closes the elementary path of the oxygen surface diffusion. As a result the isotopic exchange preferentially occurs via easy flipping of the oxygen atoms within the surface peroxy intermediate without explicit formation of energetically more costly oxygen vacancies.

The quantum chemical modeling of H_2 molecule activation and subsequent surface dehydroxylation was performed for the bare and ROS covered (100) termination. Following the available data on hydrogen interaction with oxide surfaces [40, 41], a H_2 dissociative adsorption on the lattice oxygen anions or the suprafacial ROS species was considered. For H_2 activation on bare surface we selected two vicinal anionic $O_{2O,1T}$ sites (Fig. 6a) with the interionic distance of 2.95 Å, suitable for sizeable overlap between the corresponding H_2 and O^{2-} orbitals. In the proposed scenario the hydrogen molecule with the initial equilibrium H–H bond length of $d_{H–H} = 0.75$ Å, while approaching the $O_{2O,1T}$ surface sites is stretched to 1.23 Å upon reaching the transition state geometry (Fig. 6b). In a slightly asymmetric TS significant interaction between the surface oxygens and the both hydrogen atoms takes place, with the incipient bond lengths of 1.14 and 1.17 Å. The energetic cost of this step was equal to 1.11 eV, and the final product

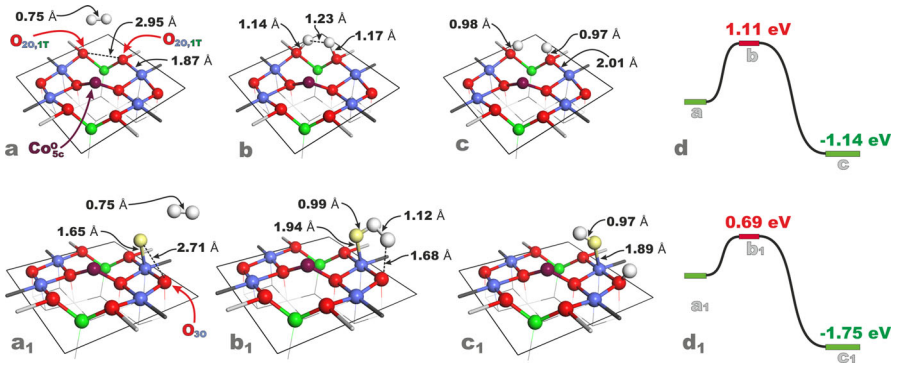

Fig. 6 The topmost layer atomic composition of the (1 × 1) surface elements of the consecutive steps of hydrogen activation on bare (**a**–**c**) and ROS covered (**a_1**–**c_1**) cobalt spinel (100) surface. *Left panels* shows initial structure, *middle panels* transition state geometries, whereas *right panels* final structures. The reactions energetics is shown in panel **d**, **d_1**. Color coding as follows: hydrogen: *white*, cobalt oxide oxygen: *red*, oxygen adatom: *yellow*; exposed tetrahedral cobalt: *violet*, tetrahedral cobalt in first subsurface: *green*, octahedral cobalt: *blue*. (Color figure online)

with two surface hydroxyls pointing toward each other (Fig. 6c) was significantly more stable than gas phase hydrogen ($\Delta E_{reac.} = -1.14$ eV). Analysis of the charges and the magnetic moments revealed that both hydrogen adatoms moieties exhibit total Bader charge of about 0.5 $|e|$ and null magnetic moment, which is characteristic of H^+ cation. The energetics of the H_2 activation step was summarized in the corresponding energy diagram (panel **6d**).

Analogous hydrogen activation for oxygen covered surface was modeled with previously described $Co^{O}–^{18}O^{-}$ metal-oxo adducts (Fig. $6a_1$) with the shortest distance to the adjacent lattice oxygen ($d_{O–O} = 2.71$ Å), which is beneficial for H_2 molecule activation. The transition state for hydrogen attachment (Fig. $6b_1$) is not symmetrical. As a result, the O–H bond formed between the hydrogen and the oxygen adatom is essentially formed ($d_{O–H}$ equals 0.99 Å), whereas the distance between the second H atom and the lattice oxygen is quite large ($d_{O–H} = 1.68$ Å), showing rather small interaction. Both H–H and Co–O bond lengths are stretched comparing to their initial state (by 0.36 and 0.30 Å, respectively), but the energetic effort for this deformation is largely compensated by the energetic gain due to O–H bond formation. This gives rise to quite low activation energy of 0.69 eV (nearly twice lower than the corresponding value for the surface O^{2-} sites). The transition state can be described as H_2 activated on the O adatom, and its slight bending toward the lattice oxygen is responsible for appearance of final double hydroxyl structure shown in Fig. $6c_1$, which is 1.75 eV more stable than the gas phase H_2. Both suprafacial and intrafacial stabilized hydrogens exhibit the charge of about +0.5 $|e|$, consistent with their protonic nature. The energetics of this reaction activation step was briefly summarized in the diagram (Fig. $6d_1$).

The hydroxylated surface states produced according to both activation mechanism (Fig. 6c, c_1) were chosen as starting points for molecular modeling of surface dehydroxylation. In the interfacial mechanism, formation of H_2O involves extraction of the lattice oxygen, thus the resultant dehydroxylated surface contains

an oxygen vacancy. Mechanistic details of this process are shown in Figs. 7a–c, with the transition state presented in the middle panel. During the reaction one of the OH groups (right in Fig. 7a) is shifted towards the second hydrogen maintaining the initial O–H distance of 0.98 Å. The O–Co bonds are strongly elongated from 1.98 to 2.21 Å (Co^{T}–O) and from 2.01 to 2.42 Å (Co^{O}–O). The second hydrogen is only slightly moved from its initial O_{surf} site ($d_{O–H} = 1.1$ Å), and the formation of H–O bond is not launched at this point ($d_{O–H} = 1.69$ Å). Such reorganization of initial bonds is energetically costly and requires 1.71 eV. The resultant atomic configuration of the relaxed surface after final formation of H_2O is shown in Fig. 7c, where the vacancy is indicated as a yellow cube. In the vicinity of the created defect, shortening of the Co–O bonds from 1.98 to 1.89 Å took place, and the energy is enhanced to 1.35 eV with respect to initial hydroxylated state of the surface. A dominant part of this value is contributed by the energy required for the oxygen vacancy formation ($E_{vac}^{O_2} = 0.91$ eV) [28]. The energy diagram of this step is presented in Fig. 7d.

For the (100) surface of cobalt spinel covered by the suprafacial oxygen atoms, the dehydroxylation process does not involve lattice oxygen atoms since water can be produced by association of surface hydroxyl and surface stabilized H^+ species (Fig. 7a_1). Transition state for this mechanism (Fig. 7b_1) shows that only slight shift of the hydrogen stabilized on the O_{3O} centers together with small elongation of the H–O_{3O} and Co–O bonds (from 0.99 to 1.19 Å and from 1.90 to 2.14 Å, respectively) are required to pass the energy barrier ($\Delta E_{act} = 1.15$ eV). The final state of this route is shown in Fig. 7c_1, and the reaction energy equals 1.01 eV (Fig. 7d_1), being substantially smaller than in the previous case. As a result the suprafacial dehydroxylation being kinetically and thermodynamically much more favorable than the intrafacial one may operate even at relatively low temperatures

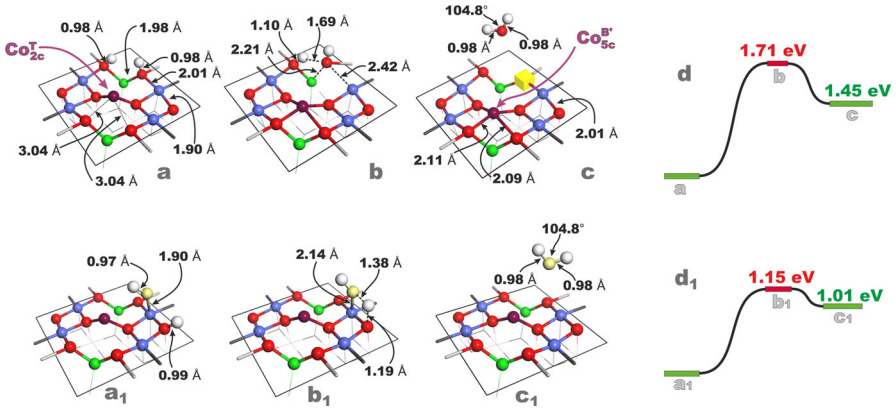

Fig. 7 The topmost layer atomic composition of the (1 × 1) surface elements showing subsequent frames of surface dehydroxylation from initially bare (**a**–**c**) and initially ROS covered (**a_1**–**c_1**) cobalt spinel (100) surface. *Left panels* shows initial structure, middle panels transition state geometries, whereas right ones final structures. The reactions energetics is shown in panel **d**, **d_1**. Color coding as follows: hydrogen: *white*, cobalt oxide oxygen: *red*, oxygen adatom: *yellow*; exposed tetrahedral Co: *violet*, tetrahedral cobalt in first subsurface: *green*, octahedral cobalt: *blue*. (Color figure online)

(below 300–350 °C). The appearance of significant amount of $H_2^{16}O$ in the reaction products is thus associated with the fast isotopic $^{18}O/^{16}O$ scrambling in the transient peroxo intermediates, and is not diagnostic of involvement of the Mars–van Krevelen mechanism. The intrafacial dehydroxylation, in turn, is energetically costly due to the oxygen vacancy formation. When such mechanism dominates production of $H_2^{16}O$ and $H_2^{18}O$ is not expected to be commensurate, but the presence of $H_2^{16}O$ is now indicative for the Mars-van Krevelen mechanism.

Conclusions

Pulse $^{16}O_2/^{18}O_2$ isotopic exchange and TPSR of hydrogen oxidation on the cobalt spinel nanocatalyst were investigated in detail and corroborated by periodic spin unrestricted DFT-PW91+U molecular modeling. Detailed analysis of the experimental and theoretical results revealed that catalytic activity of the cobalt spinel surface is strongly associated with the presence of various oxygen species such as superoxo (Co^O–$(O_2)^-$–Co^O, peroxo (Co^T–$(O_2)^{2-}$–Co^O), monoatomic metaloxo (Co^T–O, Co^O–O), and oxygen vacancies (V_O), which appear in different temperature windows. The diatomic species stable below 160 °C are reluctant to isotopic exchange, and exhibit lower reactivity toward hydrogen (E_{act} = 16 kcal/mol) in comparison to monoatomic species, highly reactive in isotopic exchange and H_2 oxidation (E_{act} = 9 kcal/mol). Surface diffusion of monoatomic oxygen along the Co^O and $O^{2-}_{2O,1T}$ sites is responsible for formation of transient peroxy $(^{18}O$–$^{16}O_{2O,1T})^{2-}$, and easy flipping of the suprafacial (top) and intrafacial (bottom) oxygen atoms. Small activation energy of 0.39 eV leads to facile isotopic exchange, without explicit formation of energetically more costly oxygen vacancies. It was also shown that monoatomic species are not only more active in H–H bond activation (E_{act} of 1.15 eV) than lattice oxygens (E_{act} = 1.71 eV), but also give rise to more facile dehydroxylation, as in the latter case dehydroxylation is not accompanied by oxygen vacancy formation. The appearance of significant amount of $H_2^{16}O$ in the reaction products is associated with the facile isotopic $^{18}O/^{16}O$ scrambling in the transient peroxo intermediates, and is not diagnostic of involvement of the Mars-van Krevelen mechanism.

Acknowledgements This work was supported by the financial support of Polish National Science Center Grant No. DEC-2011/03/B/ST5/01564.

References

1. H. Sun, H.M. Ang, M.O. Tadé, S. Wang, J. Mater. Chem. A **1**, 14427 (2013)

2. X. Xie, W. Shen, Nanoscale **1**, 50 (2009)
3. L.F. Liotta, H. Wu, G. Pantaleo, A.M. Venezia, Catal. Sci. Technol. **3**, 3085 (2013)
4. J. Petryk, E. Kolakowska, Appl. Catal. B Environ. **24**, 121 (2000)
5. E. Finocchio, G. Busca, V. Lorenzelli, V.S. Escribano, J. Chem. Soc. Faraday Trans. **92**, 1587 (1996)
6. L.F. Liotta, G. Di Carlo, G. Pantaleo, G. Deganello, Appl. Catal. B Environ. **70**, 314 (2007)
7. Y. Liu, D.C. Higgins, J. Wu, M. Fowler, Z. Chen, Electrochem. Commun. **34**, 125 (2013)
8. Z. Chromčáková, L. Obalová, F. Kovanda, D. Legut, A. Titov, M. Ritz, D. Fridrichová, S. Michalik, P. Kuśtrowski, K. Jirátová, Catal. Today **257**, 18 (2015)
9. K. Asano, C. Ohnishi, S. Iwamoto, Y. Shioya, M. Inoue, Appl. Catal. B Environ. **78**, 242 (2008)
10. Y. Takita, T. Tashiro, Y. Saito, F. Hori, J. Catal. **97**, 25 (1986)
11. G. Maniak, P. Stelmachowski, A. Kotarba, Z. Sojka, V. Rico-Pérez, A. Bueno-López, Appl. Catal. B Environ. **136–137**, 302 (2013)
12. P. Broqvist, I. Panas, H. Persson, J. Catal. **210**, 198 (2002)
13. W. Piskorz, F. Zasada, P. Stelmachowski, A. Kotarba, Z. Sojka, Catal. Today **137**, 418 (2008)
14. L.F. Liotta, M. Ousmane, G. Di Carlo, G. Pantaleo, G. Deganello, G. Marci, L. Retailleau, A. Giroir-Fendler, Appl. Catal. A Gen. **347**, 81 (2008)
15. J.-B. Li, Z.-Q. Jiang, K. Qian, W.-X. Huang, Chin. J. Chem. Phys. **25**, 103 (2012)
16. N. Bahlawane, Appl. Catal. B Environ. **67**, 168 (2006)
17. A. Bielański, J. Haber, *Oxygen in Catalysis* (Marcel Dekker, New York, 1991)
18. D.V. Ivanov, E.M. Sadovskaya, L.G. Pinaeva, L.A. Isupova, J. Catal. **267**, 5 (2009)
19. C. Doornkamp, M. Clement, V. Ponec, J. Catal. **182**, 390 (1999)
20. K. Klier, J. Nováková, P. Jíru, J. Catal. **2**, 479 (1963)
21. E. Heracleous, A.A. Lemonidou, J. Catal. **237**, 175 (2006)
22. Z. Sojka, Catal. Rev. Sci. Eng. **37**, 461 (1995)
23. X.-Y. Pang, C. Liu, D.-C. Li, C.-Q. Lv, G.-C. Wang, ChemPhysChem **14**, 204 (2013)
24. H.-F. Wang, R. Kavanagh, Y.-L. Guo, Y. Guo, G. Lu, P. Hu, J. Catal. **296**, 110 (2012)
25. X.-L. Xu, E. Yang, J.-Q. Li, Y. Li, W.-K. Chen, ChemCatChem **1**, 384 (2009)
26. D. Gamarra, A. López Cámara, M. Monte, S.B. Rasmussen, L.E. Chinchilla, A.B. Hungría, G. Munuera, N. Gyorffy, Z. Schay, V. Cortés Corberán, J.C. Conesa, A. Martínez-Arias, Appl. Catal. B Environ. **130–131**, 224 (2013)
27. J. Kaczmarczyk, F. Zasada, J. Janas, P. Indyka, W. Piskorz, A. Kotarba, Z. Sojka, ACS Catal. **6**, 1235 (2016)
28. F. Zasada, W. Piskorz, J. Janas, J. Gryboś, P. Indyka, Z. Sojka, ACS Catal. **5**, 6879 (2015)
29. S. Selcuk, A. Selloni, J. Phys. Chem. C **119**, 9973 (2015)
30. F. Zasada, W. Piskorz, Z. Sojka, J. Phys. Chem. C **119**, 19180 (2015)
31. G. Henkelman, B.P. Uberuaga, H. Jónsson, J. Chem. Phys. **113**, 9901 (2000)
32. http://theory.cm.utexas.edu/vtsttools/
33. V.G. Hadjiev, M.N. Iliev, I.V. Vergilov, J. Phys. C: Solid State Phys. **21**, L199 (1988)
34. W. Piskorz, F. Zasada, P. Stelmachowski, A. Kotarba, Z. Sojka, J. Phys. Chem. C **117**, 18488 (2013)
35. W. Piskorz, F. Zasada, P. Stelmachowski, O. Diwald, A. Kotarba, Z. Sojka, J. Phys. Chem. C **115**, 22451 (2011)
36. H.-F. Wang, R. Kavanagh, Y.-L. Guo, Y. Guo, G. Lu, P. Hu, J. Catal. **296**, 110 (2012)
37. F.F. Tao, J.-J. Shan, L. Nguyen, Z. Wang, S. Zhang, L. Zhang, Z. Wu, W. Huang, S. Zeng, P. Hu, Nat. Commun. **6**, 7798 (2015)
38. F. Zasada, W. Piskorz, S. Cristol, J.-F. Paul, A. Kotarba, Z. Sojka, J. Phys. Chem. C **114**, 22245 (2010)
39. C. Michel, E. Baerends, J. Inorg. Chem. **48**, 3628 (2009)
40. S. Chrétien, H. Metiu, J. Phys. Chem. C **119**, 19876 (2015)
41. Y. Wei, U. Martinez, L. Lammich, F. Besenbacher, S. Wendt, Surf. Sci. **619**, L1 (2014)